

Spherical Harmonics Microwave Algorithm for Shape and Location Reconstruction of Breast Cancer Tumor

Magda El-Shenawee¹ and Eric Miller²

¹Department of Electrical Engineering

University of Arkansas, Fayetteville AR 72701

²Center for Subsurface Sensing and Imaging Systems (CenSSIS)

Department of Electrical and Computer Engineering

Northeastern University, Boston MA 02115

magda@uark.edu, elmiller@ece.neu.edu

Abstract

A reconstruction algorithm to simultaneously estimate the shape and location of three-dimensional breast cancer tumor is presented and its utility is analyzed. The approach is based on a spherical harmonic decomposition to capture the shape of the tumor. We combine a gradient descent optimization method with a direct electromagnetic solver to determine the coefficients in the harmonic expansion as well as the coordinates of the center of the tumor. The results demonstrate the potential advantage of collecting data using a multiple-view/tomographic-type strategy. We show how the order of the harmonic expansion must be increased to capture increasingly “irregularly” shaped tumors and explore the resulting increase in the CPU time required by the algorithm. Our approach shows accurate reconstruction of the tumor image regardless of the source polarization. This work demonstrates the promise of the algorithm when used on data corrupted with Gaussian noise and when perfect knowledge of the tumor electrical properties is not available.

I. Introduction

Promising results concerning the use of microwave imaging for early detection of breast cancer have been reported recently in the literature [1-8] where the potential for resolving tumors as small as 5 mm has been demonstrated. However, the existing systems still suffer from major limitations which present considerable challenges toward moving this technology into the clinic. One such challenge is the difficulty in distinguishing between responses of benign and malignant tumors. As discussed in [5] and [9], some benign tumors may also have high water content and could produce a scattering response similar to that generated by malignant tumors. Fortunately, benign and malignant tumors differ significantly in shape as demonstrated in Figure 2 in chapter 21 of the *Molecular Biology of the Cell* [10], in which it shows the shape of an adenoma (a benign glandular tumor) and an adenocarcinoma (a malignant glandular tumor). As discussed in [10], there are many forms that such tumors may take; however, that figure illustrates schematically types that might be found in the breast. As demonstrated in [10], the benign tumors tend to have smooth spherical shape while malignant tumors tend to have irregular non-spherical shapes due to the random and invasive nature of malignant cells growth.

As second challenge associated with the use of microwave imaging concerns the nature of the problem to be solved. When used to recover a fine scale, voxelated or tessellated representation of the breast, typical inverse methods must solve a highly ill-posed, nonlinear inverse problem. As indicated in the previous paragraph, for the breast imaging problem however, one may not be so interested in such an image, but rather in retrieving from the data information directly related to the shape of the tumor. As shown in [11], such information can in fact be captured using far few parameters than is required in a voxel-based reconstruction thereby resulting in an inverse problem that is in a sense easier to solve.

The current work provides an investigation of an efficient microwave algorithm to simultaneously reconstruct the shape and location of breast tumors using near incident waves that propagate into the breast tissue and scatter due to the presence of a tumor. The scattered fields are received in the near-zone at all polarizations using several point receivers [12].

The preliminary results of the current study are intended to address several key issues regarding using the microwave imaging techniques to reconstruct the shape and location of breast tumor. The results presented here are obtained using a two-region simplified model of the breast that consists of the healthy breast tissue and the tumor tissue. A perfect matching medium surrounding the breast with the same electrical properties of breast tissue is assumed here to minimize the reflection from air/breast skin interface [3], [6], [13]. Also the skin thickness of the breast will not be accounted for in the presented model [13]. On the other hand, the breast inhomogeneity, due to the presence of fat and glandular tissue, will require implementing a fast forward solver capable of computing scattered fields from inhomogeneous medium (e.g. the fast multipole multilevel method), which is not the focus of this work but will be the emphasis of a separate investigation.

The irregular shape of the 3-D tumor is modeled using the spherical harmonics technique similar to the work by Garboczi, in which aggregates in concrete were simulated using the spherical harmonic functions [14]. Fig. 1 shows the configuration of the two-region breast model assuming the patient is lying prone.

A variety of algorithms for imaging have been developed for two-dimensional (2-D) or 3-D dielectric, conducting or perfect electric conducting objects (PEC) in both the time- and frequency- domains [15-37]. The frequency-domain algorithms generally estimate either the electrical properties of the object (i.e., the real and imaginary parts of the relative permittivity)

[16-30], or the shape and/or location of the object (assuming an *a priori* knowledge of its dielectric constants) [31-32]. Most of the published frequency-domain work for shape reconstruction is focused on 2-D PEC or dielectric objects [33-35], with few exploring 3-D shape reconstruction of PEC objects [37], in which the object location was *a priori* assumed known.

The focus of the current work is to simultaneously reconstruct the shape and location of 3-D dielectric lossy objects of arbitrary shape and location immersed in lossy medium. The basic idea here is to implement a steepest descent gradient technique to minimize a cost functional searching for the shape and location parameters of a tumor present in normal breast tissue. The incident fields are calculated in the near-zone based on the model of point current source given in [38], while the scattered fields are also computed in the near-zone using the method of moments (MoM) upon computing the surface currents [39].

The flowchart of the presented imaging algorithm is shown in Fig. 2 and will be discussed in Section II. In Section III, the numerical results will demonstrate the advantage of using the multiple-view strategy that indeed improves the convergence of the imaging algorithm towards the true tumor. We believe that this strategy helps the algorithm to avoid being trapped in local minima similar to the advantage of using the frequency-hopping strategy [17]. The algorithm will also be tested on corrupted synthetic data using additive white Gaussian noise [26].

As shown in Fig. 2, the algorithm requires calling the forward solver many times to numerically calculate the gradient of the cost function with respect to each shape and location parameter. This represents a major computational disadvantage for inverse scattering problems especially for recovering large number of parameters. In particular, if the dielectric constant at each pixel in the breast is to be estimated to reconstruct the image of the tumor; using this algorithm will require excessive CPU time. The advantage here is that the tumor's irregular

shape can be modeled using few parameters based on the spherical harmonic functions. The disadvantage is the need for *a priori* assumption of the electrical properties of the breast and tumor tissue. The results demonstrated the potential of the algorithm when a perfect knowledge of the tumor's properties is not available; however, imperfect knowledge of breast tissue properties will lead to imperfect matching with the surrounding medium and it will cause unwanted reflections from the breast.

II. Formulations

As mentioned earlier, we assume that the breast is surrounded by a perfectly matching medium, the normal breast tissue is homogeneous except for the tumor tissue, and the breast skin thickness is ignored [3], [6], [13]. In this scenario, the electromagnetic waves will scatter only due to the presence of a tumor inside the breast. The reconstruction algorithm presented here involves combining two techniques; the forward solver to calculate the scattered fields (i.e. the direct method) and an optimization technique based on the steepest descent gradient method for minimizing a cost functional (i.e. the error function) [40-42]. Due to the small size of the scatterer (i.e. the breast tumor) in the current model, the MoM is considered a reasonable method for the forward solver since we need only solve for the surface currents on the tumor. A brief discussion of the incident, scattered, tumor model, and the algorithm will be given here.

A. The near-field solution for the incident wave

The model of a current point source located at the origin and directed in the z-direction is given by $\bar{J} = J_0 e^{j\omega t} \delta(x) \delta(y) \delta(z) \mathbf{a}_z$ [38], where J_0 and $\omega = 2\pi f$ are the amplitude and the angular frequency of the current source, respectively. This source produces near fields at point P given by [38]:

$$E_r = \frac{J_0 e^{-\gamma r}}{4\pi} \left(\sqrt{\frac{\mu}{\varepsilon}} \frac{2}{r^2} + \frac{2}{j\omega\varepsilon r^3} \right) \cos \vartheta \quad (1a)$$

$$E_\vartheta = \frac{J_0 e^{-\gamma r}}{4\pi} \left(\frac{j\omega\mu}{r} + \sqrt{\frac{\mu}{\varepsilon}} \frac{1}{r^2} + \frac{1}{j\omega\varepsilon r^3} \right) \sin \vartheta \quad (1b)$$

$$H_\varphi = \frac{J_0 e^{-\gamma r}}{4\pi} \left(\frac{\gamma}{r} + \frac{1}{r^2} \right) \sin \vartheta \quad (1c)$$

where (r, ϑ, φ) are the spherical coordinate system of point P and $\gamma = j\omega\sqrt{\mu\varepsilon}$ is the propagation constant of the wave. The permeability and permittivity of the medium are $\mu = \mu_0$ and $\varepsilon = \varepsilon_0\varepsilon_r$, respectively, where μ_0 and ε_0 are the permeability and permittivity of the free space. For a lossy medium, the relative permittivity is complex given by $\varepsilon_r = \varepsilon' - j\sigma/(\omega\varepsilon_0)$, where σ is the conductivity of the medium. This source also represents an infinitesimal dipole aligned in the z -direction where the effect of changing its direction to the x - or y - directions will be investigated in Section III.

B. The forward scattering model

The electric fields scattered from the tumor are calculated using the MoM which involves discretizing the tumor surface S_T into patches using the RWG triangular patches (Raw, Wilton, Glisson) [39]. Upon applying the boundary conditions, arrive at a linear system of equations to be solved to obtain the unknown electric and magnetic surface current coefficients \bar{I}_T . The system of equations is given by [39]:

$$\bar{Z}_{T,T} \bar{I}_T = \bar{V}_T \quad (2)$$

The impedance matrix $\bar{Z}_{T,T}$ incorporates the interactions between elements on the tumor surface and the vector \bar{V}_T represents the tangential components of the incident electric and normalized

magnetic fields on the tumor surface obtained from (1). A brief summary of the formulations is given in Appendix A.

C. The Spherical harmonic model

We used the spherical harmonic functions to model the irregular shape of the tumor where the radius at each point on the tumor surface is a function of the spherical angles θ and ϕ [14]. This model is restricted to star convex objects, which implies that any line segment from the center of the star to the surface is contained inside the object [43]. The radius $r(\theta, \phi)$ is given as [14]:

$$r(\theta, \phi) = \sum_{n=0}^{\infty} \sum_{m=-n}^n a_{nm} Y_n^m(\theta, \phi), \quad 0 \leq \theta \leq \pi, \quad 0 \leq \phi \leq 2\pi \quad (3a)$$

in which a_{nm} are the harmonic coefficients and the function $Y_n^m(\theta, \phi)$ is the spherical harmonic function given by [14]:

$$Y_n^m(\theta, \phi) = \sqrt{\frac{(2n+1)(n-m)!}{4\pi(n+m)!}} P_n^m(\cos(\theta)) e^{jm\phi} \quad (3b)$$

The functions $P_n^m(x)$ are the associated Legendre functions which are a set of orthogonal polynomials of order n . The radius $r(\theta, \phi)$ will be re-written here as (see Appendix B):

$$r(\theta, \phi) = r_0 \left\{ 1 + r_1 \cos(\theta) + r_2 \sin(\theta) \cos(\phi) + r_3 \sin^2(\theta) \cos(2\phi) + r_4 \sin(\theta) \cos(\theta) \cos(\phi) + \dots \right\} \quad (3c)$$

where r_0, r_1, r_2, \dots represent the spherical harmonic coefficients to be retrieved to reconstruct the shape of the 3-D object. These new coefficients have the constraints that $r_0 > 0$ and $|r_i| \leq 1$, for $i = 1, 2, 3, \dots$, to insure generating a 3-D object of a main radius r_0 added to it several harmonics of radii r_i . Notice that the 3-D object becomes exactly a sphere of radius r_0 when all other coefficients are zeros (i.e. $r_i = 0$, for $i = 1, 2, 3, \dots$).

D. The reconstruction algorithm

The basic idea is to use a gradient-based optimization technique to search for the unknown coefficients r_i for $i = 0, 1, 2, 3 \dots$, and the tumor center coordinates (x_0, y_0, z_0) . The flowchart of the algorithm is shown in Fig.2. The initial guess of the object is assumed a sphere of radius r_0 and location at x_0, y_0, z_0 . The initial guesses of the radius and location are obtained using uniformly distributed random numbers generated between the upper and lower limits of radius and location. These limits are realistically defined by the location of the source/receivers around the breast as shown in Fig. 1. An appropriate cost function to be minimized is defined by the error between the measurement and the simulated fields given by:

$$C(\Theta) = \sum_{i=1}^{N_r} \left| \overline{E}_i^{Meas.} - \overline{E}_i^{Sim} \right|^2 \quad (4a)$$

in which, $\overline{E}_i^{Meas.}$ and \overline{E}_i^{Sim} represent the scattered complex electric fields obtained from measurement (synthetic data) and simulated data, respectively. The subscript i represents the receiver's number, where N_r is the total number of point receivers. The vector Θ represents the unknown parameters to be estimated. The number of elements in vector Θ varies according to the chosen number of spherical harmonic functions in (3c). The cost function in (4a) is to be minimized until an acceptable error is achieved.

A rapid steepest descent optimization approach, developed by Fletcher and Powell [41-42], is implemented to minimize the cost function $C(\Theta)$. The estimated vector $\hat{\Theta}$ is obtained as:

$$\hat{\Theta} = \arg_{\Theta} (\min(C(\Theta))) \quad (4b)$$

in which the elements of the unknown vector Θ will be restricted to an upper and lower bound constraints which will be *a priori* provided ($\Theta_{LB} \leq \Theta \leq \Theta_{UB}$). The basic form of the iterative inversion technique (without the constraints) is given by [41-42]:

$$\hat{\Theta}_{k+1} = \hat{\Theta}_k + \alpha_k d_k \quad (4c)$$

in which k is the iteration number, α is a small enough positive scalar value represents the step at iteration k , and the vector d_k is the vector that minimizes the quadratic equation $q(d)$ [41-42]:

$$q(d) = 0.5d^T H_k d + c^T d, \quad d \in R^n \quad (4d)$$

in which R is the real domain, $c = \nabla C(\hat{\Theta}_k)$ is the gradient of the cost function $C(\Theta)$, and the matrix H contains the true curvature information for the feasible region and can be regarded as a reduced inverse Hessian matrix [41-42]. Equations (4) show that reconstructing the 3-D tumor requires solving the forward problem large number of times, either to compute \bar{E}_i^{Sim} at each receiver in (4a) or to compute the gradient $c = \nabla C(\hat{\Theta}_k)$ in (4d) with respect to each parameter of vector Θ . Calculating the gradient is a key computational issue of this algorithm, which is implemented here using the forward finite difference approximations [44]. The shape of the 3-D tumor becomes more irregular upon increasing the number of spherical harmonics in (3c), leading to increase in the required CPU time as will be demonstrated in Section III.

III. Numerical Results

In this section, we demonstrate the efficiency of the algorithm using several numerical examples. Several point sources and receivers are located around the breast as shown in Fig. 1. In all examples presented here, the sources and receivers are transmitting or receiving waves from four views around the breast described as (with $0 \geq z_0 \geq -20$ cm):

- (1) View1: $x_0 = -5$ cm and -5 cm $\leq y_0 \leq 25$ cm , (2) View2: $y_0 = 25$ cm and -5 cm $\leq x_0 \leq 25$ cm ,
- (3) View3: $x_0 = 25$ cm , -5 cm $\leq y_0 \leq 25$ cm , (4) View4: $y_0 = -5$ cm and -5 cm $\leq x_0 \leq 25$ cm

In all results presented here, the source frequency is assumed 6 GHz. Based on several numerical examples, it is observed that a maximum number of iterations ranging from 30 to 50

per view is reasonable. In this work, the upper and lower constraints on the object location are: $5\text{cm} \leq x_0 \leq 15\text{cm}$, $5\text{cm} \leq y_0 \leq 15\text{cm}$, $-5\text{cm} \leq z_0 \leq -15\text{cm}$, while the constraints on the object's radii are: $0.25\text{cm} \leq r_0 \leq 5\text{cm}$, $0 \leq r_i \leq 0.45$, $i = 1, 2, 3 \dots$ (noting that r_i has no units, see eq. 3c). The amplitude of the point current source in (1) is $J_0 = 1 \text{ mA}$ and is aligned in the z-direction unless otherwise is stated [38]. All computations are conducted using the HP DS25 (COMPAQ ALPHA) EV68/1000MHz server. The examples considered here are summarized in Table 1.

Table 1 Summary of numerical examples

| Figure | Purpose | Figure | Purpose |
|--------|--|---------|---|
| Fig. 3 | Marching vs simultaneous views | Fig. 8 | Imperfect knowledge of tumor's $\hat{\epsilon}_r$ |
| Fig. 4 | Seven parameters with $r_0 = 2\text{cm}$ | Fig. 9 | Source polarization effect |
| Fig. 5 | Seven parameters with $r_0 = 1\text{cm}$ | Fig. 10 | Data corrupted with Gaussian noise |
| Fig. 6 | Seven parameters with $r_0 = 5\text{mm}$ | Fig. 11 | Data contains unknown clutter |
| Fig. 7 | Thirteen parameters with $r_0 = 1.75\text{cm}$ | | |

(i) Algorithm Strategy

The flowchart of the algorithm is shown in Fig. 2 and it proceeds as follows; (i) the initial guesses of tumor radius and position are generated randomly with assuming the tumor as a sphere by setting all harmonic coefficients to zero, (ii) the point sources and receivers are arranged according to View1 shown in Fig. 1b, (iii) the algorithm is executed for certain number of iterations (30-50 iterations per view in this work), (iv) the cost function is updated at each iteration, (v) T/R pairs are rotated to View 2 as shown in Fig. 1c is utilized with updating the initial guess from the results obtained in View 1. This mechanism is repeated using View 3 and View4. This reconstruction algorithm represents a “*marching on in view*” technique.

The true tumor is generated in all cases using 360 RWG patches and 182 surface nodes; however, the reconstruction algorithm is set to use only 270 RWG patches and 137 nodes in generating the reconstructed tumor in each inversion iteration. This implies that using different

MoM discretization and different numbers of the spherical harmonics render the synthetic data to be non-ideal and more realistic.

(ii) Marching on in views vs simultaneous views

The use of a gradient descent approach brings with it a host of difficulties in terms of local minima. Global methods which avoid these problems (in theory) are well studied but still rather intensive. Reports in the literature indicate that various methods of cycling through the data can help avoid local minima while still allowing us to employ the relatively straightforward gradient descent optimization method. Here we seek to understand through experiments the merits of these choices in the context of the breast imaging problem at hand.

In this example, we examine three options of inverting data collected using point transmitters/receivers (T/R) located around the target. For simplicity, a sphere of radius 2.5 cm and relative dielectric constant $\epsilon_r = 50 - j12$ immersed in air will be used as the target. The true sphere is located at $x_0 = 7.5\text{cm}$, $y_0 = 6.35\text{ cm}$, and $z_0 = -10\text{cm}$. The resolution of the point T/R locations is $\sim 0.468\text{ cm}$ in the x - or y - directions and $\sim 0.625\text{ cm}$ in the z -direction as described earlier. These three options are summarized as:

- (1) Option 1 is to simultaneously invert using data collected from all T/R pairs, i.e. using $4 \times 1088 = 4352$ pairs located at all four views (solid line in Fig. 3).
- (2) Option 2 is to invert data collected using 1088 sources located at View1 and receiving simultaneously at all $4 \times 1088 = 4352$ receiver located at all four views. Then use the rotated 1088 sources at View2 and simultaneously receive at all 4352 receiver located at all four views, etc. The parameters estimated using the sources at View1 are used as initial guess for the rotated sources at View2, etc (dashed-line in Fig. 3).

(3) Option 3 is to invert data collected using only 1088 T/R pairs at a time, where the sources are located at View1 and the receivers are located at the opposite side (View3). This means that 1088 T/R pairs are used for 30 iterations and then rotated simultaneously as shown in Fig. 1, etc. (dot-dashed-line in Fig. 3).

In Figs. 3a-d, four randomly generated initial guess of the sphere radius and location (r_0, x_0, y_0, z_0) are presented as: 1.225, 6.865, 9, -11.5 cm in Fig. 3a, 0.443, 12.3, 6.34, -6.5 cm in Fig. 3b, 3.57, 8.05, 9.1, -7 cm in Fig. 3c, and 0.77, 11.3, 8.4, -14.4 cm in Fig. 3d.

The results of Fig. 3 show the potential of the algorithm to invert data based on options 2 and 3. Sometimes a temporary increase in the error function is observed upon changing the view; however ultimately it reduces and convergence is achieved. The reconstructed spheres show very good agreement with the true one (not presented here). It seems that this strategy helps the algorithm to avoid being trapped in local minima similar to the advantage of using the frequency-hopping strategy [17]. Based on these results, we have adopted the strategy of *marching on in view* (Option 3) in the remainder of this work.

(iii) Reconstruction of arbitrary shape and location

In all remainder examples, the two-region model of the breast with an immersed tumor will be used. In Example 2, the true tumor is generated using seven unknown coefficients including four spherical harmonics and three unknowns for the center location (x_0, y_0, z_0) . At 6 GHz, the healthy and malignant breast tissues are assumed to have relative dielectric constants of $\epsilon_r = 9 - j1.2$ and $50 - j12$, respectively, [5]. At this frequency, the wavelength in breast tissue is approximately 1.6 cm. The true tumor is non-spherical as shown in Fig. 4 with true parameters as $r_0 = 2\text{cm}$, $r_1 = 0.678$, $r_2 = 0.495$, $r_3 = 0.11$ (see eq. 3c) and true location at $x_0 = 13.35\text{cm}$, $y_0 = 11.95\text{cm}$, $z_0 = -8.5\text{cm}$. Several initial guesses are successfully examined; however,

the specific initial guesses in Fig. 4 are $r_0 = 3.57\text{cm}$, $x_0 = 8.05\text{cm}$, $y_0 = 9.1\text{cm}$, $z_0 = -7\text{cm}$ with all higher order harmonic coefficients initially set to zeros ($r_1=r_2=r_3 = 0$). The reconstructed tumor is obtained using seven unknowns in Fig. 4b and five unknowns in Fig. 4c. The true tumor is shown in black and the reconstructed tumor is shown in red. The normalized cost function is plotted in Fig. 4a for both cases showing the reduction in the error upon increasing the inversion iterations. The results show good agreement between the reconstructed and true tumor in both cases. The CPU time required for reconstructing the tumor in Fig. 4b and 4c is $\sim 12\text{-}13$ hrs.

To show the capability of the algorithm in reconstructing smaller tumors, the same data of Fig. 4 are used in Figs. 5 and 6 but for tumors with $r_0 = 1\text{cm}$ in Fig. 5 and $r_0 = 5\text{mm}$ in Fig. 6. As shown in the flow chart of Fig. 2, the convergence of the algorithm could be achieved if the change in the cost function is less than a tolerance of $10^{-6}\text{-}10^{-8}$ or if the maximum number of iterations is reached (50 in this example). The results of Figs. 5 and 6 show the potential of the algorithm in reconstructing smaller tumors.

Example 3 will demonstrate the reconstruction of a tumor of more irregular shape as shown in Fig. 7. The true tumor is generated using thirteen parameters with true values as: $r_0 = 1.75\text{cm}$, $r_1 = 0.365$, $r_2 = 0.266$, $r_3 = 0.059$, $r_4 = 0.217$, $r_5 = 0.282$, $r_6 = 0.162$, $r_7 = 0.322$, $r_8 = 0.265$, $r_9 = 0.025$ (see eq. 3c) and location at $x_0 = 11.5\text{cm}$, $y_0 = 6.45\text{cm}$, $z_0 = -7.5\text{cm}$. The reconstruction is based on using four parameters in Fig. 7b (i.e. a sphere), seven parameters in Fig. 7c, and thirteen parameters in Fig. 7d.

Notice that the cost function associated with the thirteen-parameter reconstruction is smaller than that of the four or the seven-parameter reconstructions. Also, as expected using the thirteen parameters in the reconstruction potentially provides more accurate reconstruction of the tumor shape. It is interesting to observe that in this example when the reconstruction has been initially

attempted for the thirteen parameters; no convergence was achieved. However, when the reconstruction was conducted using four parameters (i.e. a sphere) and then using the estimated values of r_0, x_0, y_0, z_0 as initial guess for the thirteen unknown reconstruction; a good agreement with the true tumor is obtained as shown in Fig. 7d. It is observed that initially using only four unknowns in the reconstruction leads to accurate estimation of the location x_0, y_0, z_0 , while re-iterating the algorithm using more parameters leads to more accurate reconstruction of the shape upon comparing Fig. 7d with 7b. This conclusion is consistent with the work by Tortel and Saillard in [37]. The total CPU time for Fig. 7b is ~24 hrs, for Fig. 7c is ~ 21 hrs, and for Fig. 7d is ~22 hrs (without including the CPU time required for Fig. 7b).

(iv) Imperfect knowledge of tumor's electrical properties

In all examples presented earlier, the complex dielectric constant of the tumor is *a priori* assumed known. The effect of imperfect knowledge of the tumor's electrical properties is examined in Example 4. The true value of the tumor's complex dielectric constant at 6 GHz, as used to generate all synthetic data, is $\epsilon_r = 50-j12$ [5]. The true tumor generated using seven unknowns and reconstructed using five unknowns of Example 2 (Fig. 4) is used here. The relative error in the estimated parameters is expressed as $\|\hat{\Theta} - \Theta^{True}\|_2 / \|\Theta^{True}\|_2$, where $\|\cdot\|_2$ represents the norm-2, $\hat{\Theta}$ represents the estimated vector parameters of the reconstructed tumor and Θ^{True} represents the true vector parameters. This error is plotted in Fig. 8a vs the error in the tumor's complex dielectric constant $\hat{\epsilon}_r$. In this example, Θ^{True} has a length of seven while $\hat{\Theta}$ has a length of five (see Fig. 4), therefore zero padding is used to make the two vectors of equal lengths (i.e. r_2 and r_3 are assumed zeros in $\hat{\Theta}$). The zero value in the axis of $\hat{\epsilon}_r$ in Fig. 8a represents the perfect knowledge of the true dielectric constant (similar to Fig. 4), while the

positive or the negative values of $\hat{\varepsilon}_r$ implies imperfect knowledge with larger or smaller values of the true ε_r , respectively. Notice that a relative error in the reconstruction $\sim 17\%$ (in the vertical-axis) is associated with the zero error in ε_r . This can be explained by the fact that the reconstruction is based on using only five parameters instead of seven parameters which causes an error of only 7%. The results of Figs. 8b-c show that the algorithm has a potential of providing good reconstruction of the tumor with uncertainty in its dielectric constant up to $\pm 20\%$ which implies that $\hat{\varepsilon}_r = 40-j8$ for the -20% error and $\hat{\varepsilon}_r = 60-j14.4$ for the +20% error. This can be explained by the fact that even with $\pm 20\%$ error in $\hat{\varepsilon}_r$, still there is a large contrast between the electrical properties of the tumor and the surrounding medium ($\varepsilon_r = 9-j1.2$) [5].

(v) Effect of source polarization

In all results presented in this section, the current source is assumed in the z -direction as given in (1) which is in the vertical-direction (see Fig. 1). When the current source is oriented horizontally, it will be in the y -direction at View1 and View 3, and in the x -direction at View 2 and View 4 (see Fig. 1). Example 5 shows the reconstruction of a new tumor that has a dimension in the z -direction larger than the dimensions in the x - y cross section as shown in Fig. 9. The true tumor is generated using ten parameters with true values as: $r_0 = 1$ cm, $r_1 = 0.475$, $r_2 = 0.347$, $r_3 = 0.077$, $r_4 = 0.282$, $r_5 = 0.282$, $r_6 = 0.211$ (see eq. 3c) and location at $x_0 = 11.5$ cm, $y_0 = 6.45$ cm, $z_0 = -7.5$ cm. In this particular example, when all ten parameters of the original tumor are attempted to be recovered using random initial guesses, a convergence to the true parameters has been achieved only when vertical current sources are used. No advantage is observed when data of both vertical and horizontal current sources are used simultaneously. On the other hand, when starting the reconstruction assuming the tumor is a sphere and then using the recovered four parameters as initial guess to re-reconstruct the irregular tumor, both source polarizations

provide good image reconstruction as shown in Figs. 9b and 9c, respectively. This observation is consistent with the results of Fig. 7 and with the work by Tortel and Saillard in [37]. Notice that Fig. 9a shows a monotonic decrease in the cost function when vertical sources are used, except for View 2 where a slight increase is observed, which is not the case for the horizontal case. The later case shows a cost function error of 2.5% at View1 compared with 7.9% at View4, leading to insignificant improvement when the image is reconstructed using the parameters recovered at View1 instead of View4 (not presented here). Notice that all images presented in this work are reconstructed using the parameters recovered after four views. The results of Figs. 9b and 9c show a slight improvement in the image when using vertical sources.

(vi) Random noise added to synthetic data

In Example 6, the synthetic data obtained at 6 GHz, are corrupted by adding random Gaussian white noise. Several definitions are considered in the literature concerning adding random noise to synthetic data; however, we adopted the definition used in [26] where the signal-to-noise-ratio (SNR) is: $SNR = 10 \log_{10}(\|\bar{E}^{True} + \bar{n}\|^2 / \|\bar{n}\|^2)$ dB, where \bar{E}^{True} denotes the vector of the *noiseless* synthetic data and \bar{n} represents a complex noise vector of length $N_v N_r$, where N_v is the number of views (four in this work) and N_r is the number of receivers at each view (1088 point receivers here). The real and imaginary parts of the vector \bar{n} are generated by two independent sequences of white Gaussian variables characterized by zero mean and standard deviation σ_n . In the current work, several values of σ_n ranging from 0.001 to 0.3 are examined which gives SNR ranges from 39 to 5dB. The true tumor used in Example 2 (or Fig. 4) is also used here to investigate the effect of adding Gaussian noise on the reconstruction accuracy. The images in Fig. 10 a-d show the potential of the algorithm to reconstruct a tumor with data $SNR = 39.7$ dB, 19.8 dB, 11.3 dB and 4.9 dB, respectively.

(vii) Data contains unknown clutter

In Example 7, the background contains discrete clutters that randomly vary in size and medium. A total of twenty three small spheres are randomly generated with different radii, locations and media as shown in Fig. 11a. For simplicity, all interactions between these small scatterers and with the tumor are ignored. The data in this example are the same as in Fig. 6c with tumor's main radius $r_0 = 5\text{mm}$, $\varepsilon_r = 9 - j1.2$ for the background and $\varepsilon_r = 50 - j12$ for the tumor.

The relative dielectric constant of the first fifteen small spheres randomly ranges from 6 to 15 for the real part and from 0.5 to 1.5 for the imaginary part. To increase the level of clutter, an additional eight small spheres are added to the background with the real and imaginary parts randomly range from 5 to 40 and from 1.5 to 11, respectively. The maximum radius among all small spheres is almost 5.22% of the tumor's main radius r_0 and it occurs in the first set, while it is almost 3.73% in the additional set of eight spheres.

The data of the scattered electric fields due to the tumor and the clutter are inverted assuming that the clutter is unknown. The normalized cost functional is plotted in Fig. 11b for three cases; without clutter (same as Fig. 6c) and with clutter of fifteen and twenty three small spheres are present in the background. The reconstruction results for the clutter cases are plotted in Figs. 11c and 11d, respectively. The results in Fig. 11c show a reasonable accuracy of the algorithm even with clutter in the background, while the results in Fig. 11d show the deterioration in the accuracy as the clutter level increases.

Although all the results presented in this section are based on using 6 GHz; however, the algorithm has been successfully tested upon combining information from several frequencies

ranging from 3 GHz to 8 GHz using plane wave source (not presented here). The results were consistent with those obtained using the frequency hopping strategy [17].

IV. Conclusions

In this work, an optimization algorithm to simultaneously reconstruct the shape and location of breast cancer tumors is developed and tested. The results suggest collecting data using multiple views in the experiment to achieve the best possible reconstruction of the tumor. The algorithm shows a potential of good reconstruction of the tumor even when the synthetic data is corrupted with random Gaussian noise. In addition, increasing the number of spherical harmonics in the model leads to better capturing of the tumor shape but it takes more CPU time.

Other challenges need to be investigated such as the breast interior inhomogeneities, due to the fat and glandular tissue, and the imperfect knowledge of normal breast tissue properties. Addressing these issues will help toward the use of this technique to breast tumor imaging, which will be the focus of separate work. Another issue is that too much time is required to produce the images. This factor depends on the number of spherical harmonics utilized to reconstruct the tumor as well as the level of noise in the data. Parallel programming is one possible way to speed up the algorithm.

Appendix A

The Poggio, Miller, Chang, Harrington and Wu (the PMCHW) equations are used for dielectric scatterers [39]. The electric and magnetic surface currents (\bar{J}_T, \bar{M}_T) are related to the unknown vector coefficient \bar{I}_T through the conventional MoM approximation given by [39]:

$$\bar{J}_T(\bar{r}) = \sum_{n=1}^N I_{1n} \bar{j}_n(\bar{r}), \quad \bar{M}_T(\bar{r}) = \eta_0 \sum_{n=1}^N I_{2n} \bar{j}_n(\bar{r}), \quad \bar{r} \in S_T \quad (\text{A1})$$

in which \bar{j} is the vector basis function and $\bar{I}_T = [I_1 \ I_2]$ represents the electric and magnetic current coefficient vector, with total number of current coefficients unknown equal to $2N$. The normalization factor η_0 is the intrinsic impedance of the free space. The impedance matrix $\bar{Z}_{T,T}$ is given by [39]:

$$\bar{Z}_{T,T} = \begin{pmatrix} \langle \bar{j}, (L_1 + L_2) \bar{j} \rangle_{S_T} & \langle \bar{j}, -\eta_0 (K_1 + K_2) \bar{j} \rangle_{S_T} \\ \langle \bar{j}, \eta_0 (K_1 + K_2) \bar{j} \rangle_{S_T} & \left\langle \bar{j}, \eta_0^2 \left(\frac{L_1}{\eta_1^2} + \frac{L_2}{\eta_2^2} \right) \bar{j} \right\rangle_{S_T} \end{pmatrix} \quad (\text{A2})$$

The operators L_1 , L_2 , K_1 , and K_2 are derived in [39] and given by:

$$L_{1,2} \bar{X} = \int_{S_T} \left\{ i\omega\mu_{1,2} \Phi_{1,2} \bar{X}(\bar{r}') + \frac{i}{\omega\epsilon_{1,2}} \nabla \nabla' \cdot \bar{X}(\bar{r}') \Phi_{1,2} \right\} ds' \quad (\text{A3})$$

$$K_{1,2} \bar{X} = \int_{S_T} \bar{X}(\bar{r}') \times \nabla \Phi_{1,2} ds' \quad (\text{A4})$$

in which the 3-D scalar Green's function for region l is $\Phi_l = \exp(-ik_l |\bar{r} - \bar{r}'|) / 4\pi |\bar{r} - \bar{r}'|$ with the associated wave number $k_l = \omega \sqrt{\epsilon_l \mu_l}$. The intrinsic impedances of the two regions are η_1 and η_2 (i.e. the surrounding medium and the tumor), respectively. The complex inner product between two vector functions \bar{A} and \bar{B} is expressed by $\langle \bar{A}, \bar{B} \rangle_S = \int_S \bar{A}^* \cdot \bar{B} ds$.

Appendix B

Upon truncating the infinite summation in (3a) as:

$$r(\theta, \phi) \approx \sum_{n=0}^N \sum_{m=-n}^n a_{nm} Y_n^m(\theta, \phi), \quad 0 \leq \theta \leq \pi, \quad 0 \leq \phi \leq 2\pi \quad (\text{B1})$$

For simplicity, let $N = 4$

$$r(\theta, \phi) \approx a_{00} Y_0^0(\theta, \phi) + \sum_{m=-1}^1 a_{1m} Y_1^m(\theta, \phi) + \dots + \sum_{m=-4}^4 a_{4m} Y_4^m(\theta, \phi) \quad (\text{B2})$$

Upon substituting (3b) in (B2), we obtain

$$\begin{aligned}
r(\theta, \phi) \approx & a_{00} \sqrt{1/4\pi} P_0^0 \\
& + P_1^1 \sqrt{3/(4\pi \times 2!)} (-a_{1(-1)} e^{-j\phi} + a_{1(1)} e^{j\phi}) \\
& + P_2^2 \sqrt{5/(4\pi \times 4!)} (a_{2(-2)} e^{-j2\phi} + a_{2(2)} e^{j2\phi}) + \\
& + P_2^1 \sqrt{5/(4\pi \times 3!)} (-a_{2(-1)} e^{-j\phi} + a_{2(1)} e^{j\phi}) + \\
& + \dots \\
& + P_4^4 \sqrt{9/(4\pi \times 8!)} (a_{4(-4)} e^{-j4\phi} + a_{4(4)} e^{j4\phi})
\end{aligned} \tag{B3}$$

For the radius $r(\theta, \phi)$ to be real number, we use $a_{n(-m)} = (-1)^m a_{n(m)}$ in (B3). After some algebraic manipulations noting that P_n^m is a function of θ [14], we obtain:

$$\begin{aligned}
r(\theta, \phi) \approx & r_0 \{ 1 + r_1 \cos(\theta) + r_2 \sin(\theta) \cos(\phi) + r_3 \sin^2(\theta) \cos(2\phi) + r_4 \sin(\theta) \cos(\theta) \cos(\phi) \\
& + r_5 \cos^2(\theta) + r_6 \sin^3(\theta) \cos(3\phi) + r_7 \sin^2(\theta) \cos(\theta) \cos(2\phi) + \dots \\
& + r_{13} \sin(\theta) \cos^3(\theta) \cos(\phi) + r_{14} \cos^4(\theta) \}
\end{aligned} \tag{B4}$$

Notice that choosing $N = 4$ in (B1) provides up to fifteen r_i 's coefficients in (B4).

ACKNOWLEDGMENTS

This research was sponsored in part by the Arkansas Biosciences Institute award no. ABI-21-0103, the Women Giving Circle at the University of Arkansas grant no. WGC-22-0000, the National Science Foundation award no. ECS-0524042, and the NSF-ERC (CenSSIS) at Northeastern University award no. EEC-9986821.

References

- [1] P. M. Meaney, M. W. Fanning, D. Li, S. P. Poplack and K. D. Paulsen, "A clinical prototype for active microwave imaging of the breast," *IEEE Trans. Microwave Theory Tech.*, vol. 11, pp. 1841-1853, 2000.
- [2] P. M. Meaney, K.D. Paulsen and J. T. Chang, "Near-field microwave imaging of biologically-based materials using a monopole transceiver system," *IEEE Trans. Microwave Theory Tech.*, vol. 46, pp. 31-45, 1998.
- [3] X. Li and S. C. Hagness, "A confocal microwave imaging algorithm for breast cancer detection," *IEEE Microwave and Wireless Components Letters*, vol. 11, pp. 130-132, March 2001.
- [4] E. C. Fear and M. A. Stuchly, "Microwave detection of breast cancer," *IEEE Trans. Microwave Theory and Tech.*, vol. 46, pp. 1854-1863, November 2000.
- [5] S. Hagness, A. Taflove and J. E. Bridges, "Three-dimensional FDTD analysis of a pulsed microwave confocal systems for breast cancer detection: Design of an antenna-array element," *IEEE Trans. Antennas Propagat.*, vol. 47, pp. 783-791, May 1999
- [6] E. J. Bond, X. Li, S. Hagness and B. D. Van Veen, "Microwave imaging via space-time beamforming for early detection of breast cancer," *IEEE International Conference on Acoustics, Speech, and Signal Processing*, vol. 3, pp. 2909–2912, May 13-17, 2002.
- [7] E. C. Fear, S. C. Hagness, P. M. Meaney, M. Okoniewski, and M. Stuchly, "Enhancing breast tumor detection with near-field imaging," *IEEE Microwave magazine*, pp.48-56, March 2002.

- [8] Q. Fang, P. M. Meaney, S. D. Geimer, A. V. Streltsov and K. D. Paulsen, "Microwave image reconstruction from 3-D fields coupled to 2-D parameter estimation," *IEEE Trans. Med. Imag.*, pp. 475-484, vol. 23, no. 4, April 2004.
- [9] A. M. Campbell and D. V. Land, "Dielectric properties of female human breast tissue measures *in vitro* at 3.2 GHz," *Phys. Med. Biol.*, vol. 37, no. 1, pp. 193-210, 1992.
- [10] Bruce Alberts, Dennis Bray, Julian Lewis, Martin raff, Keith Roberts and James D. Watson, *Molecular Biology of the Cell*, Garland Publishing, Inc. New York & London, second edition, 1989.
- [11] Gregory Boverman, Ang Li, Quan Zhang, Tina Chaves, Eric L. Miller, Dana H Brooks, and David A Boas, "Quantitative Spectroscopic Diffuse Optical Tomography Guided by Imperfect A Priori Structural Information," submitted to *Physics in Medicine and Biology*, April 2005.
- [12] J. Lin and W. C. Chew, "Solution of the three-dimensional electromagnetic inverse problem by the local shape function and the conjugate gradient fast Fourier transform methods," *J. Opt. Soc. Am. A*, vol. 14, no. 11, pp. 3037-3045, November 1997.
- [13] Q. H. Liu, Z. Q. Zhang, T. T. Wang, J. A. Bryan, G. A. Ybarra, L. W. Nolte and W. T. Joines, "Active microwave imaging I-2-D forward and inverse scattering methods," *IEEE Trans. Microwave Theory and Techniques*, vol. 50, no. 1, pp. 123-133, January 2002.
- [14] E. J. Garboczi, "Three-dimensional mathematical analysis of particle shape using X-ray tomography and spherical harmonics: application to aggregates used in concrete," *Cement and Concrete Research*, vol. 32, no. 10, pp. 1621-1638, October 2002.

- [15] W. C. Chew, *Advances in Computational Electrodynamics*, chapter 12: Imaging and inverse problems in electromagnetics, Ed. A. Taflove, Artech House, Boston, pp. 653-702, 1998.
- [16] W. C. Chew and Y. M. Wang, "Reconstruction of two-dimensional permittivity distribution using the distorted Born iterative method," *IEEE Trans. Med. Imag.*, vol. 9, no. 2, pp. 218-225, December 1991.
- [17] W. C. Chew and J. H. Lin, "A frequency-hopping approach for microwave imaging of large inhomogeneous bodies," *IEEE Microwave and Guided Wave Letters*, vol. 5, no. 12, pp. 439-441, December 1995.
- [18] K. D. Paulsen, P. M. Meaney, M. J. Moskowitz and J. H. Sullivan, Jr., "A dual mesh scheme for finite element based reconstruction algorithms," *IEEE Trans. Med. Imag.*, vol. 14, no. 3, pp. 504-514, September 1995.
- [19] P. M. Meaney, K. D. Paulsen, B. W. Pogue and M. I. Miga, "Microwave image reconstruction utilizing log-magnitude and unwrapped phase to improve high-contrast object recovery," *IEEE Trans. Med. Imag.*, vol. 20, no. 2, pp. 104-116, Feb. 2001.
- [20] N. Joachimowicz, C. Pichot and J. Hugonin, "Inverse scattering: an iterative numerical method for electromagnetic imaging," *IEEE Trans. Antenn. Propag.*, vol. 39, no. 12, December 1991.
- [21] N. Joachimowicz, J. J. Mallorqui, J. Bolomey and A. Broquetas, "Convergence and stability assessment of Newton-Kantorovich reconstruction algorithms for microwave tomography," *IEEE Trans. Med. Imag.*, vol. 17, no. 4, pp. 562-570, August 1998.

- [22] A. Abubakar, R. M. van Berg and J. J. Mallorqui, "Imaging of biological data using multiplicative regularized contrast source inversion method," *IEEE Trans. Microwave Theory and Techniques*, vol. 50, no. 7, pp. 1761-1771, July 2002.
- [23] A. Abubakar, P. M. van Berg and S. Y. Semenov, "A robust iterative method for Born inversion," *IEEE Trans. Geosci. Remote Sen.*, pp. 342-354, vol. 42, no. 2, Feb. 2004.
- [24] J. T. Rekanos, T. V. Yioultsis and T. D. Tsiboukis, "Inverse scattering using the finite-element method and a nonlinear optimization technique," *IEEE Trans. Microwave Theory and Techniques*, vol. 47, no. 3, pp. 336-344, March 1999.
- [25] K. I. Schultz and D. L. Jaggard, "Microwave projection imaging for refractive objects: a new method," *J. Opt. Soc. Am. A*, vol. 4, no. 9, pp. 1773-1782, September 1987.
- [26] S. Caorsi, G. L. Gragnani, M. Pastorino, "Reconstruction of dielectric permittivity distributions in arbitrary 2-D inhomogeneous biological bodies by a multiview microwave numerical method," *IEEE Trans. Med. Imag.*, vol. 12, no. 2, pp. 232-239, June 1993.
- [27] C. Chiu and R. Yang, "Electromagnetic imaging for complex cylindrical objects," *IEEE Trans. Med. Imag.*, vol. 14, no. 4, pp. 752-756, December 1995.
- [28] A. E. Bulyshev, s. y. Semenov, A. E. Souvorov, R. H. Svenson, A. G. Nazarov, Y. E. Sizov, and G. P. Tatsis "Computational modeling of three-dimensional microwave tomography of breast cancer," *IEEE Trans. Biomed. Eng.*, vol. 48, no. 9, pp. 1053-1056, 2001.
- [29] A. Abubakar, P.M. van den Berg and S. Y. Semenov, "Two- and three-dimensional algorithms for microwave imaging and inverse scattering," *Progress In Electromagnetic Research*, vol. 37, pp. 57-79, 2002.

- [30] Z. Q. Zhang, and Q. H. Liu, "3-D nonlinear image reconstruction for microwave biomedical imaging," *IEEE Trans. Biomed. Eng.*, vol. 51, no. 3, pp. 544-548, 2004.
- [31] K. Belkebir, E. E. Kleinman and C. Pichot, "Microwave imaging—Location and shape reconstruction from multifrequency scattering data," *IEEE Trans. Microwave Theory & Techniques*, vol. 45, 4, pp. 469-476, April 1997.
- [32] E. L. Miller, M. Kilmer and C. Rappaport, "A new shape-based method for object localization and characterization from scattered field data," *IEEE Trans. Geosci. Remote Sens.*, vol. 38, pp. 1682-1696, 2000.
- [33] C. C. Chiu and Y. Kiang, "Microwave imaging of multiple conducting cylinders," *IEEE Trans. Antenn. Propag.*, vol. 40, no. 8, pp. 933-941, August 1992.
- [34] C. Chiu and Y. Kiang, "Electromagnetic inverse scattering of a conducting cylinder buried in a lossy half-space," *IEEE Trans. Antenn. Propag.*, vol. 40, no. 12, Dec. 1992.
- [35] A. Qing, "Electromagnetic imaging of two-dimensional perfectly conducting cylinders with transverse electric scattered field," *IEEE Trans. Antenn. Propag.*, vol. 50, no. 12, pp. 17861-1794, vol. 50, no. 12, December 2002.
- [36] I. T. Rekanos and T. D. Tsiboukis, "An inverse scattering technique for microwave imaging of binary objects," *IEEE Trans. Microwave Theory and Techniques*, vol. 50, no. 5, May 2002.
- [37] Herve' Tortel and Marc Saillard, "Shape reconstruction of 3D perfectly conducting object," *proceeding of the URSI-GA*, paper no 0899, July-August 2002
- [38] Donald W. Dearholt and William R. McSpadden, *Electromagnetic Wave Propagation*, McGraw-Hill Book Company, 1973.

- [39] L. Medgyesi-Mitschang, J. Putnam and M. Gedera, "Generalized method of moments for three-dimensional penetrable scatterers," *J. Opt. Soc. Am. A*, vol. 11, no. 4, pp. 1383-1398, April 1994.
- [40] M. El-Shenawee and E. Miller, "Multiple-incidence/multi-frequency for profile reconstruction of random rough surfaces using the three-dimensional electromagnetic fast multipole model," *IEEE Trans. Geosci. & Remote Sens.*, vol. 42, no. 11, pp. 2499-2510, November 2004.
- [41] R. Fletcher, "A new approach to variable metric algorithms," *The Computer Journal*, vol. 13, no. 3, pp. 317-322, August 1970.
- [42] R. Fletcher, *Practical Methods of Optimization*, volume 2, John Wiley & Son, 1981.
- [43] Eric W. Weisstein *et al.* "Star Convex." From MathWorld--A Wolfram Web Resource.
<http://mathworld.wolfram.com/StarConvex.html>
- [44] Matthew N. O. Sadiku, *Numerical Techniques in Electromagnetics*, 2nd. Ed., CRC Press LLC, Boca Raton, FL, 2001.

List of figures

Figure 1 (a) Front view of the 3-D breast two-region model, (b) top view to show the locations of the point sources and receivers, (c) top view to show the multiple-view strategy (i.e. rotation from View1 to View2, etc).

Figure 2 The flowchart of the inversion algorithm.

Figure 3 The cost function vs iteration number when simultaneously using all sources and receivers (solid-line), using marching on sources and but simultaneous use of all receivers (dashed-line), and marching on both sources and receivers (dot-dashed-line). The object is a sphere immersed in air (four unknowns r_0, x_0, y_0, z_0), with random initial guess as: (a) 1.225, 6.865, 9, -11.5 cm, (b) 0.443, 12.3, 6.34, -6.5 cm, (c) 3.57, 8.05, 9.1, -7 cm, (d) 0.77, 11.3, 8.4, -14.4 cm. The parameters of the true sphere for r_0, x_0, y_0, z_0 are 2.5, 7.5, 6.35, -10 cm, respectively.

Figure 4 Arbitrary shape tumor generated using seven unknowns, (a) the normalized cost function using seven and five parameters in the reconstruction as shown in Fig. 4b and 4c, respectively. The non-spherical true tumor has $r_0 = 2$ cm.

Figure 5 Same data of Fig. 4 but for smaller tumor with $r_0 = 1$ cm.

Figure 6 Same data of Fig. 4 but for smaller tumor with $r_0 = 5$ mm.

Figure 7 Arbitrary shape tumor generated using thirteen parameters, (a) the normalized cost function using four parameters (i.e. a sphere) in the reconstruction as shown in Fig. 7b, seven parameters in the reconstruction as shown in Fig. 7c, and thirteen parameters in the reconstruction as shown in Fig. 7d. The true r_0 is 1.75cm.

Figure 8 Imperfect knowledge of tumor's electrical properties; (a) relative error in reconstruction vs relative error in tumor's complex dielectric constant, (b) reconstruction using dielectric constant $\hat{\epsilon}_r = 40-j8$ in the algorithm (i.e. -20% error), (c) reconstruction using $\hat{\epsilon}_r = 60-j14.4$ in the algorithm (i.e. +20% error). The true value for the tumor is $\epsilon_r = 50-j12$ and the same data of Example 2 (or Fig. 4).

Figure 9 Source polarizations; vertical sources in z -direction and horizontal sources in x - or y -direction. (a) The normalized cost function vs iteration number for vertical sources (solid-line) and horizontal sources (dashed-line), (b) Tumor image using vertical sources, (c) Tumor image using horizontal sources. Both true and reconstructed tumor has ten parameters. $r_0 = 1$ cm

Figure 10 Inverting data corrupted with Gaussian noise with SNR (a) 39.7 dB, (b) 19.8 dB, (c) 11.3 dB, (d) 4.9 dB. The noiseless data are the same of Example 2 (or Fig. 4).

Figure 11 Inverting data contains unknown clutter in the background, (a) Clutter configuration, (b) Normalized cost functional using five parameters with and without clutter, (c) background contains fifteen small spheres, (d) background contains twenty three small spheres. (same data of Fig. 6).

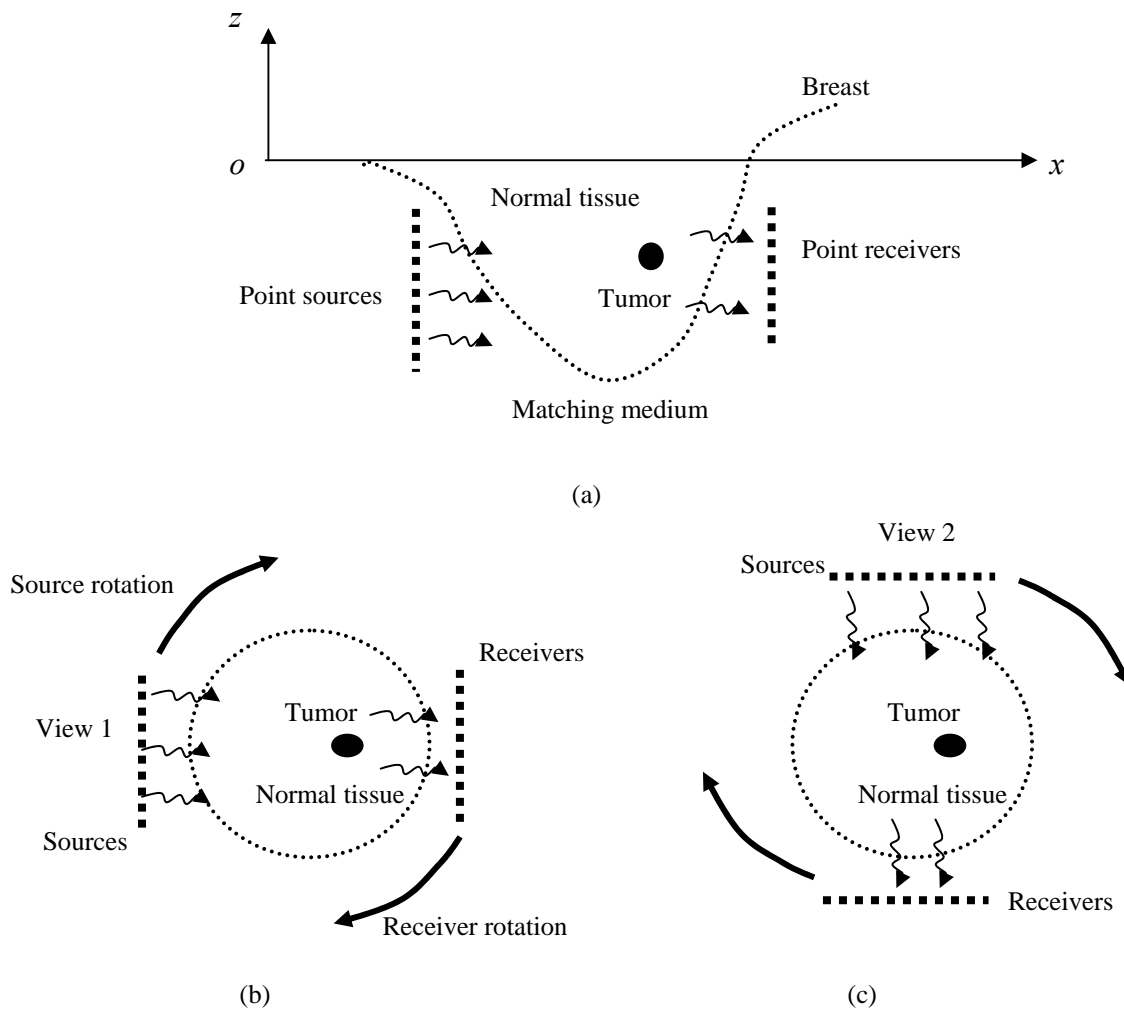


Figure 1 a-c

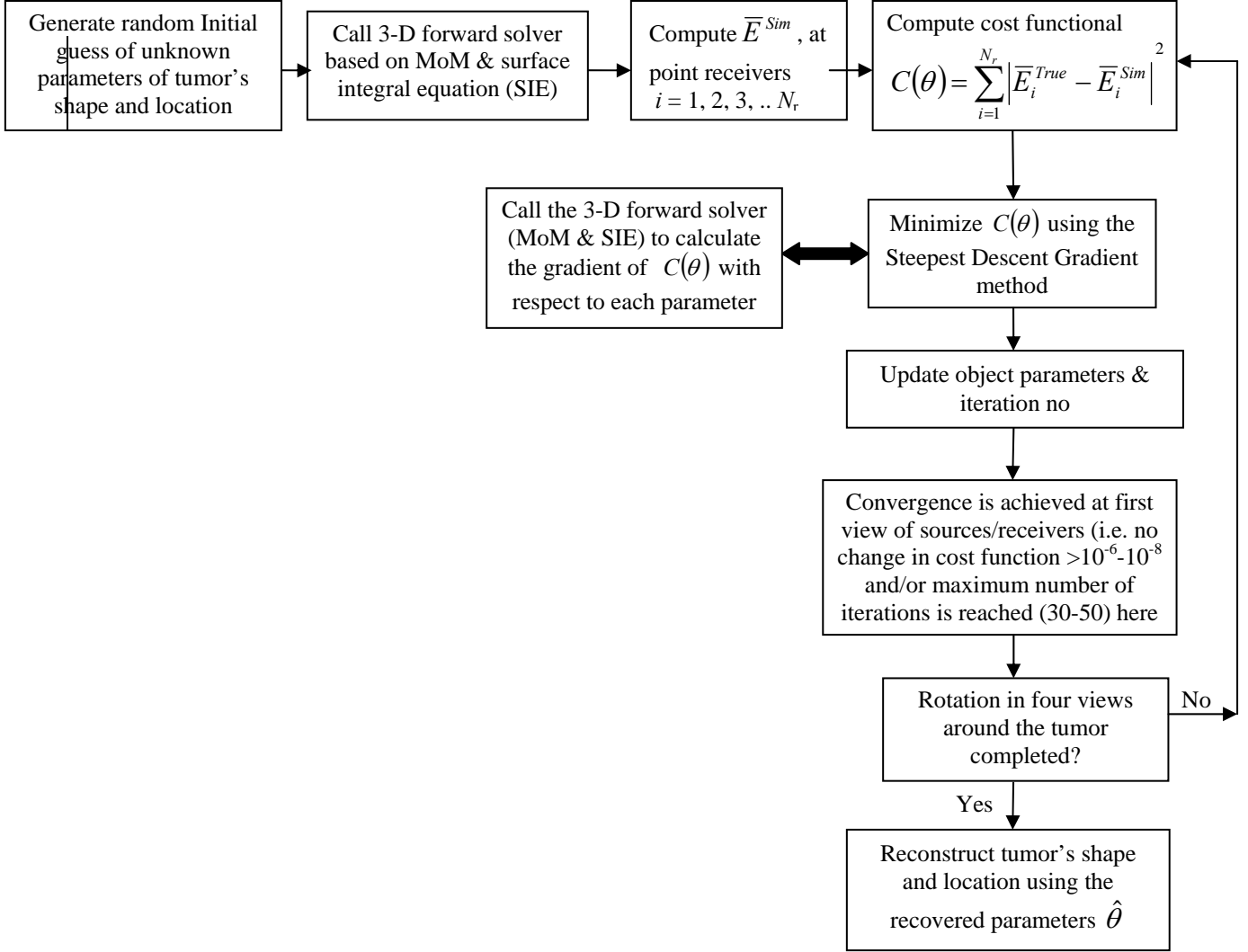


Figure 2

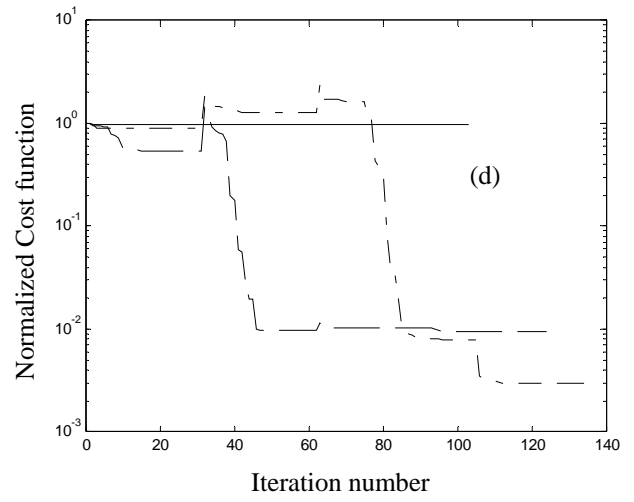
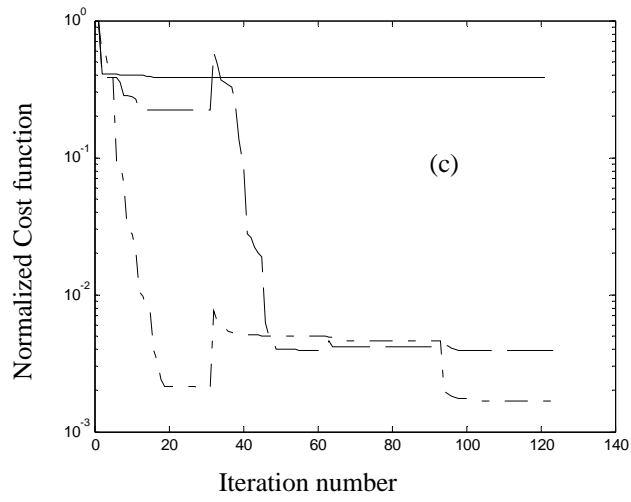
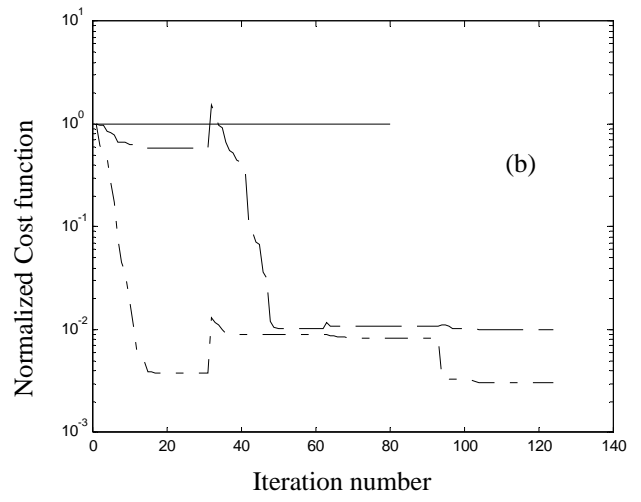
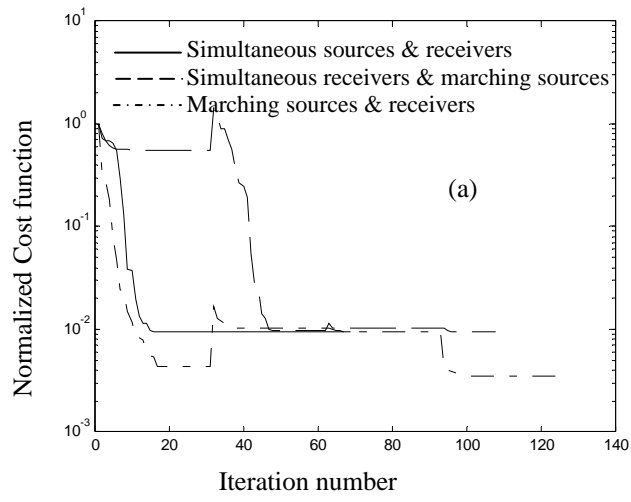


Figure 3 a-d

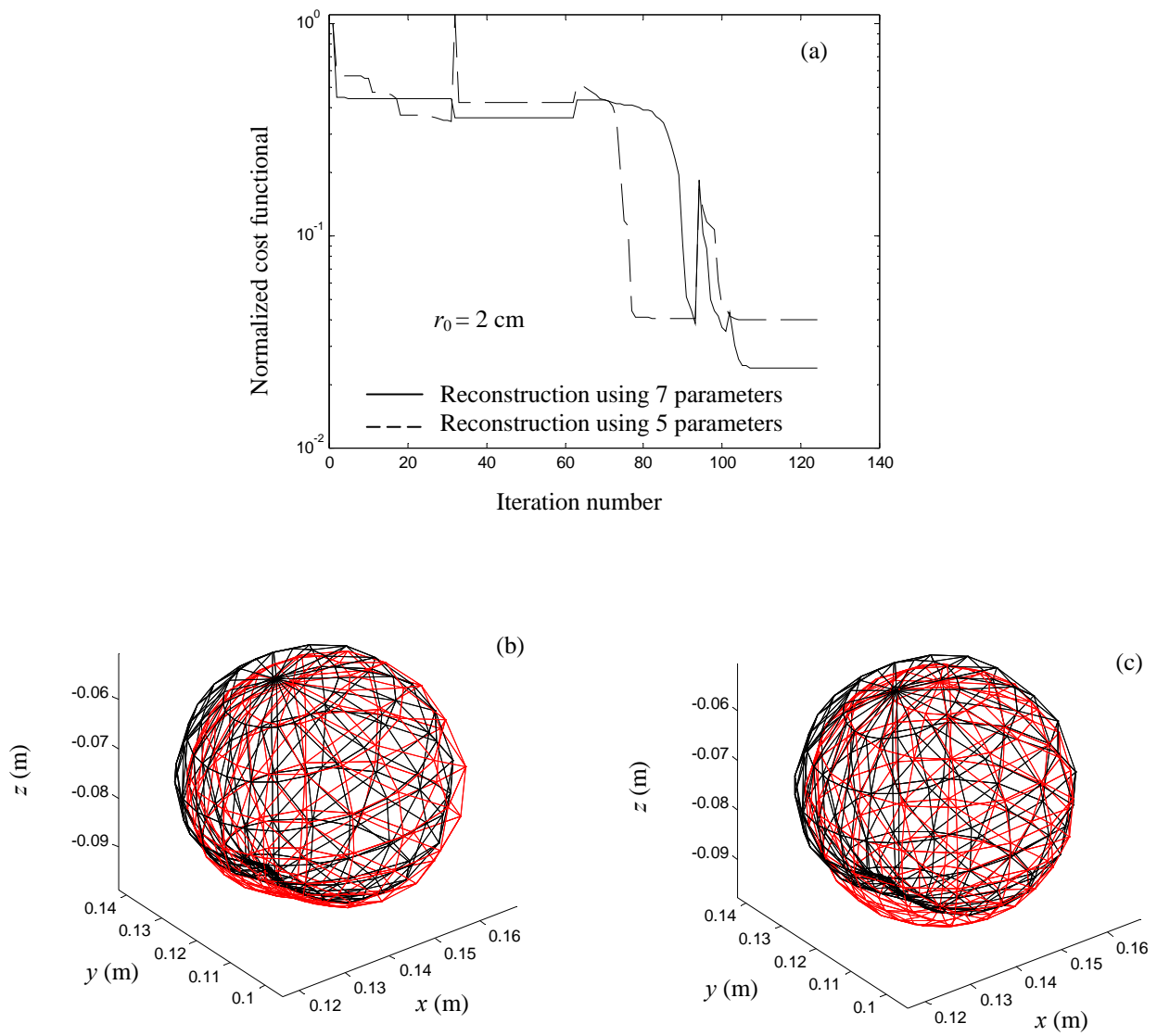


Figure 4 a-c

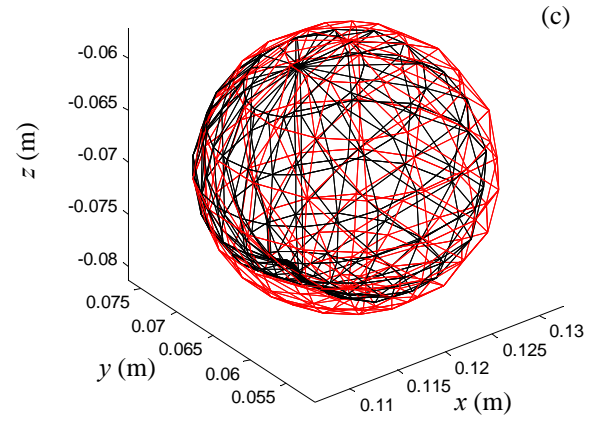
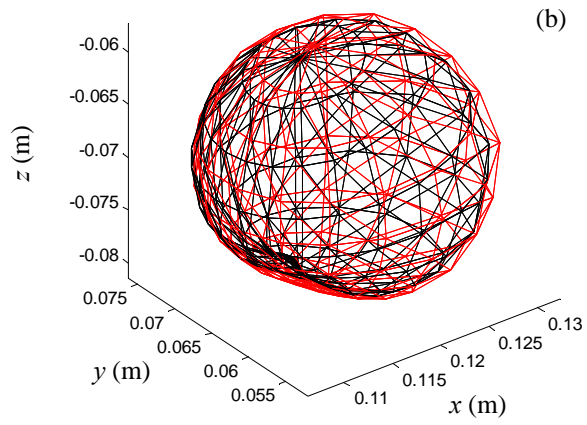
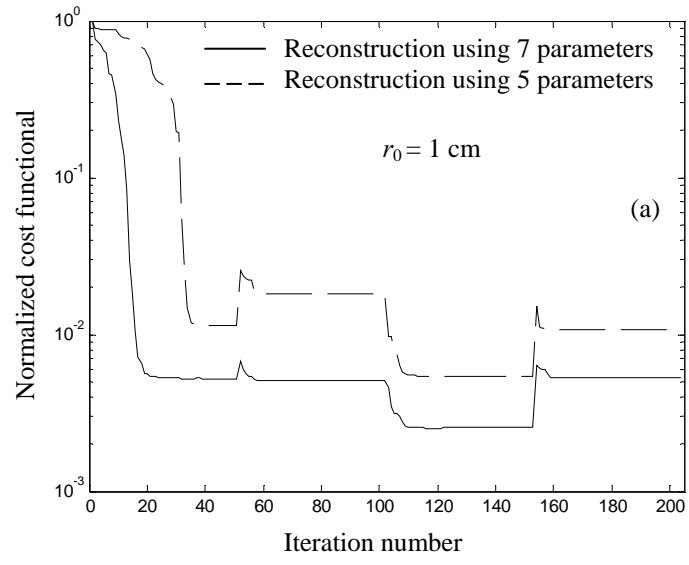


Fig.5a-c

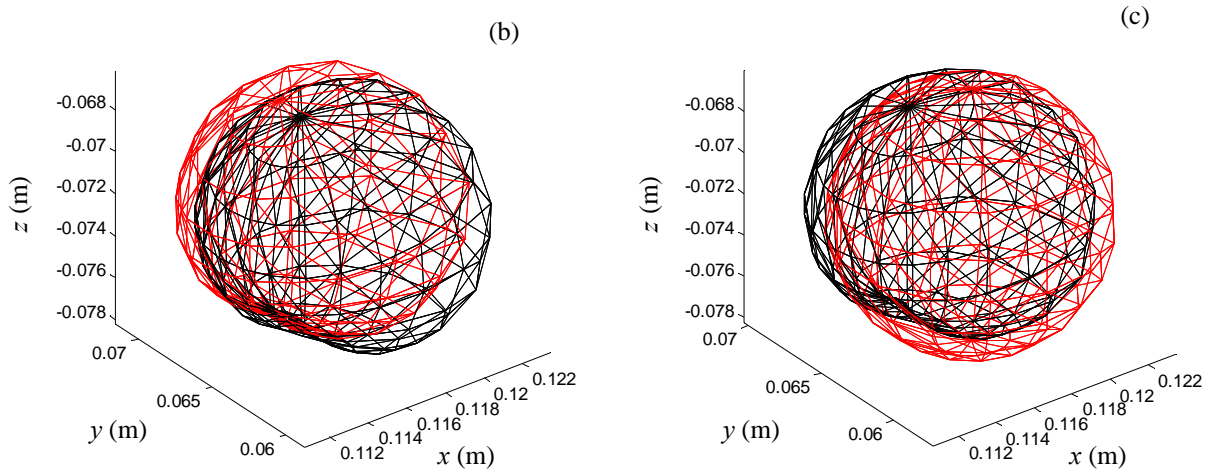
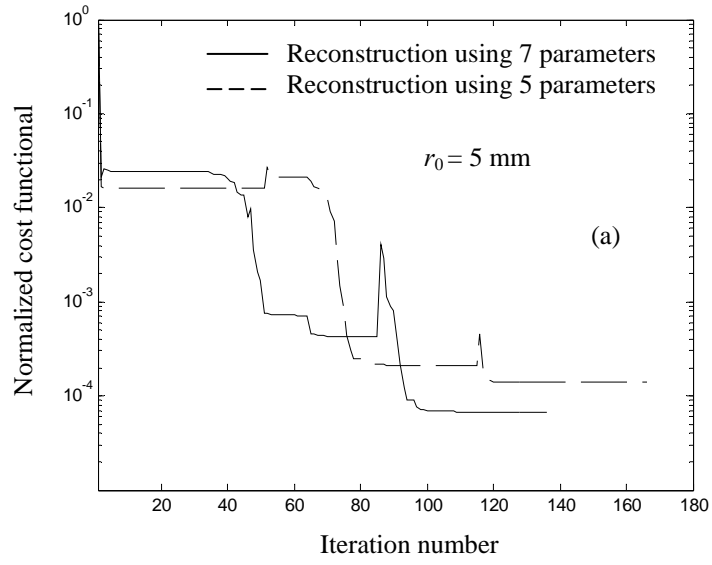


Fig. 6a-c

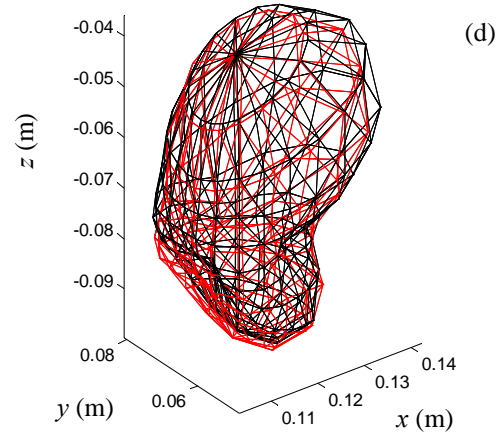
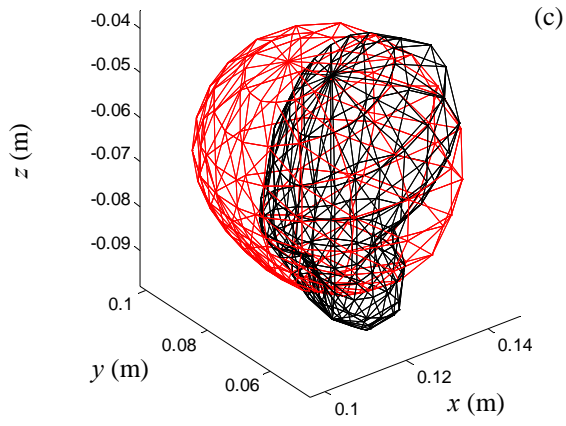
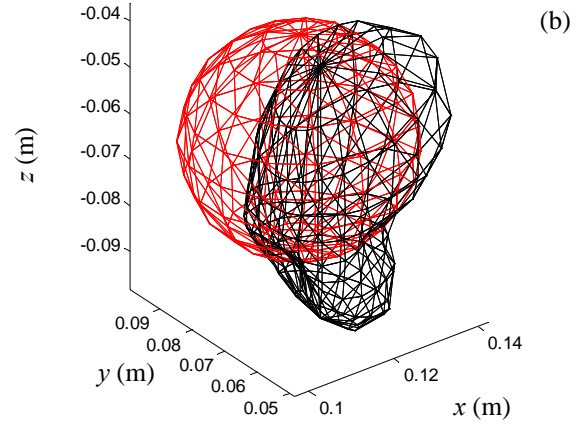
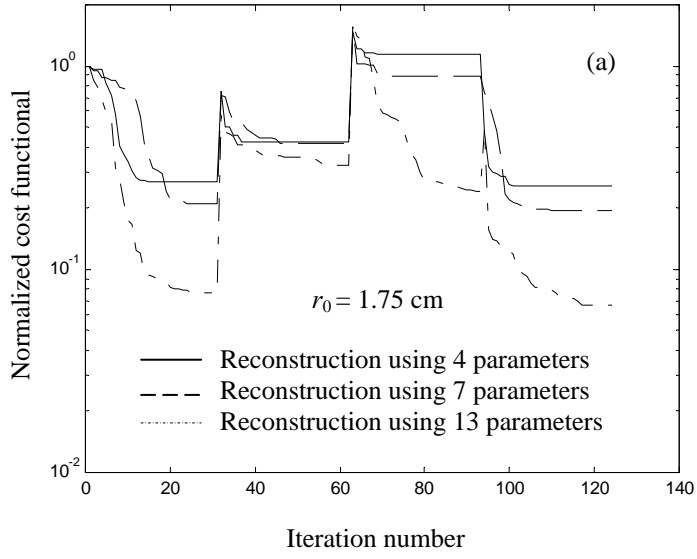


Figure 7 a-d

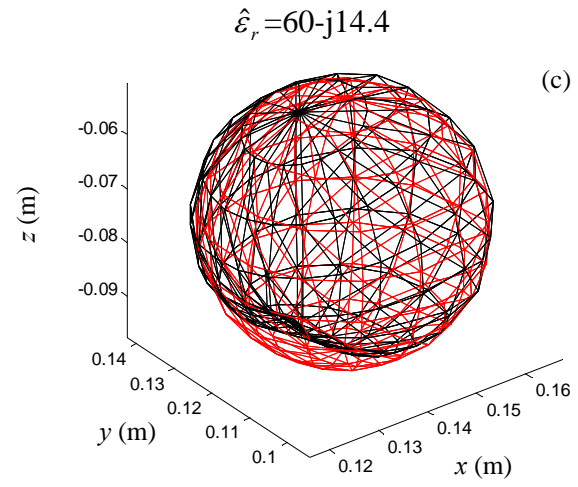
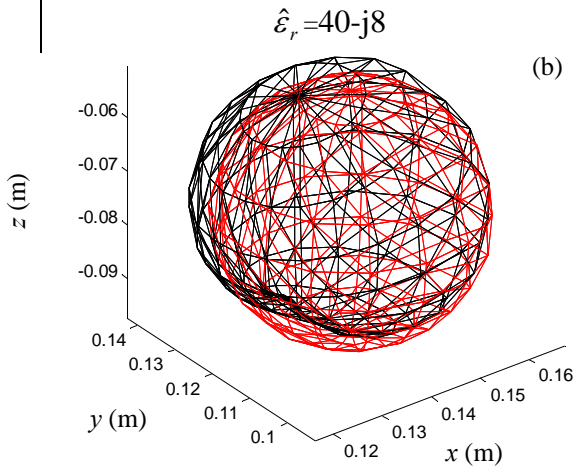
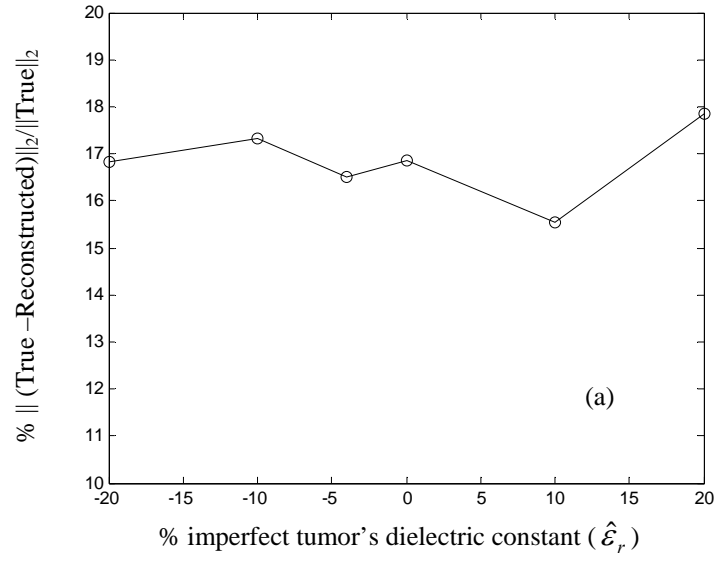


Figure 8 a-c

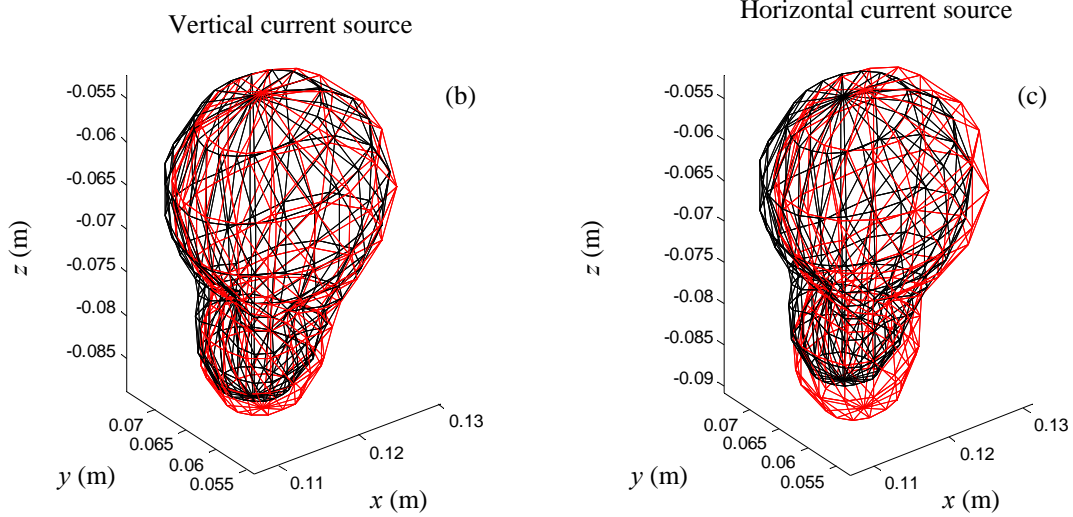
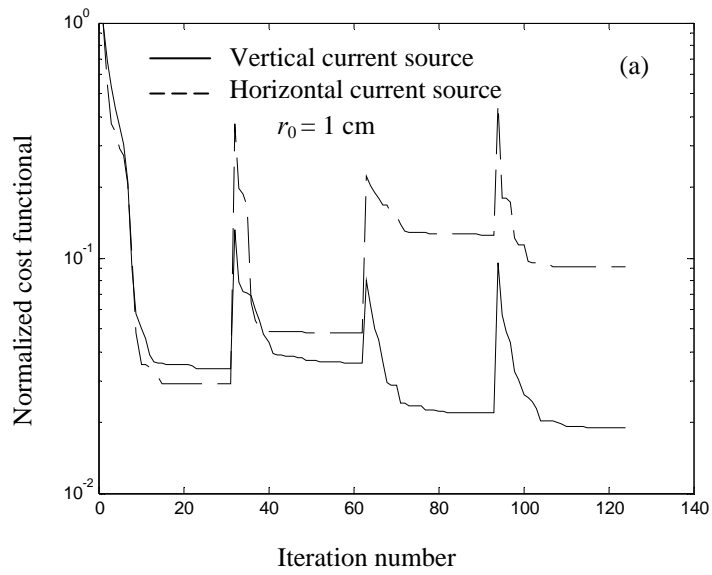


Figure 9 a-c

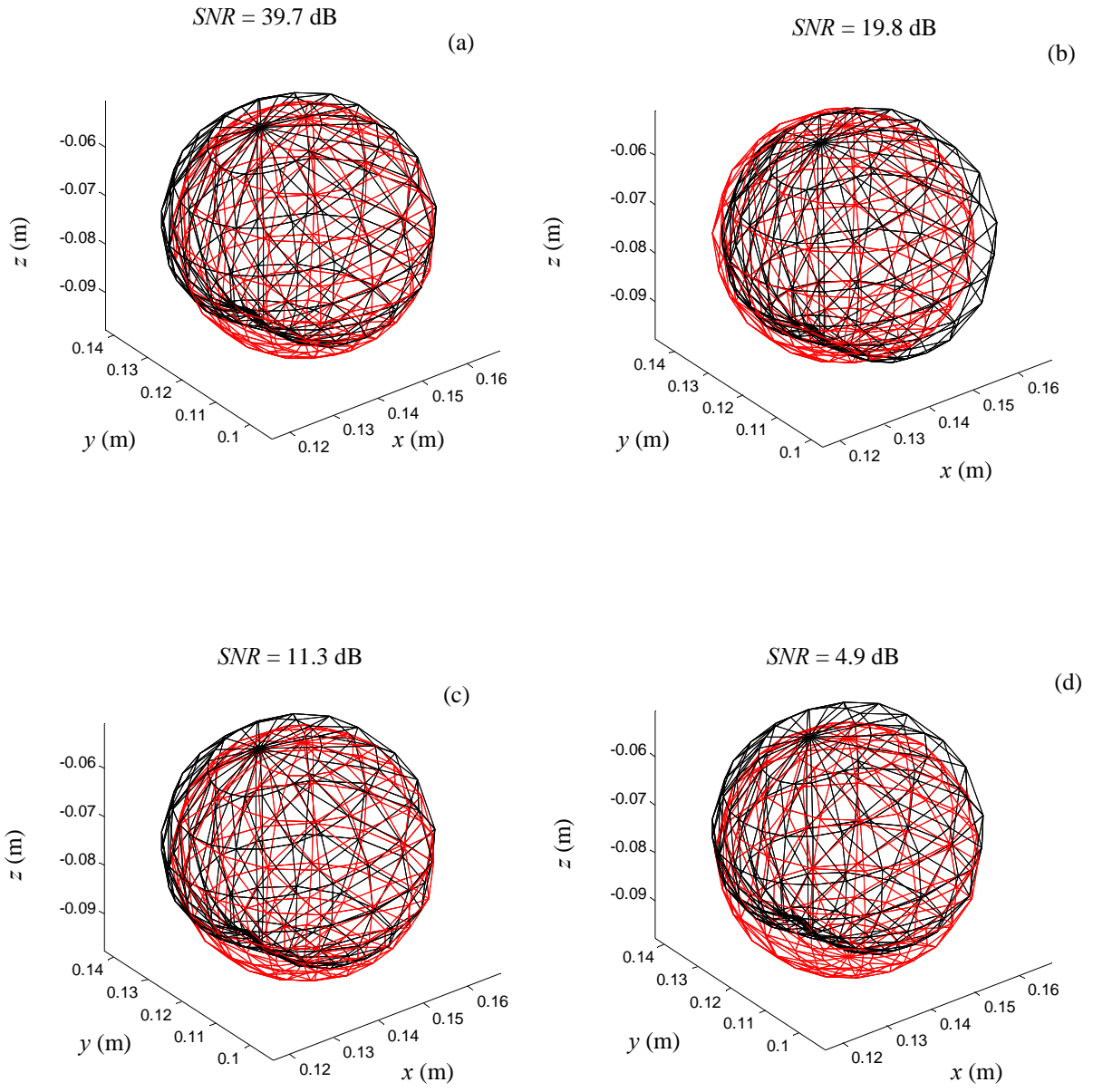


Figure 10 a-d

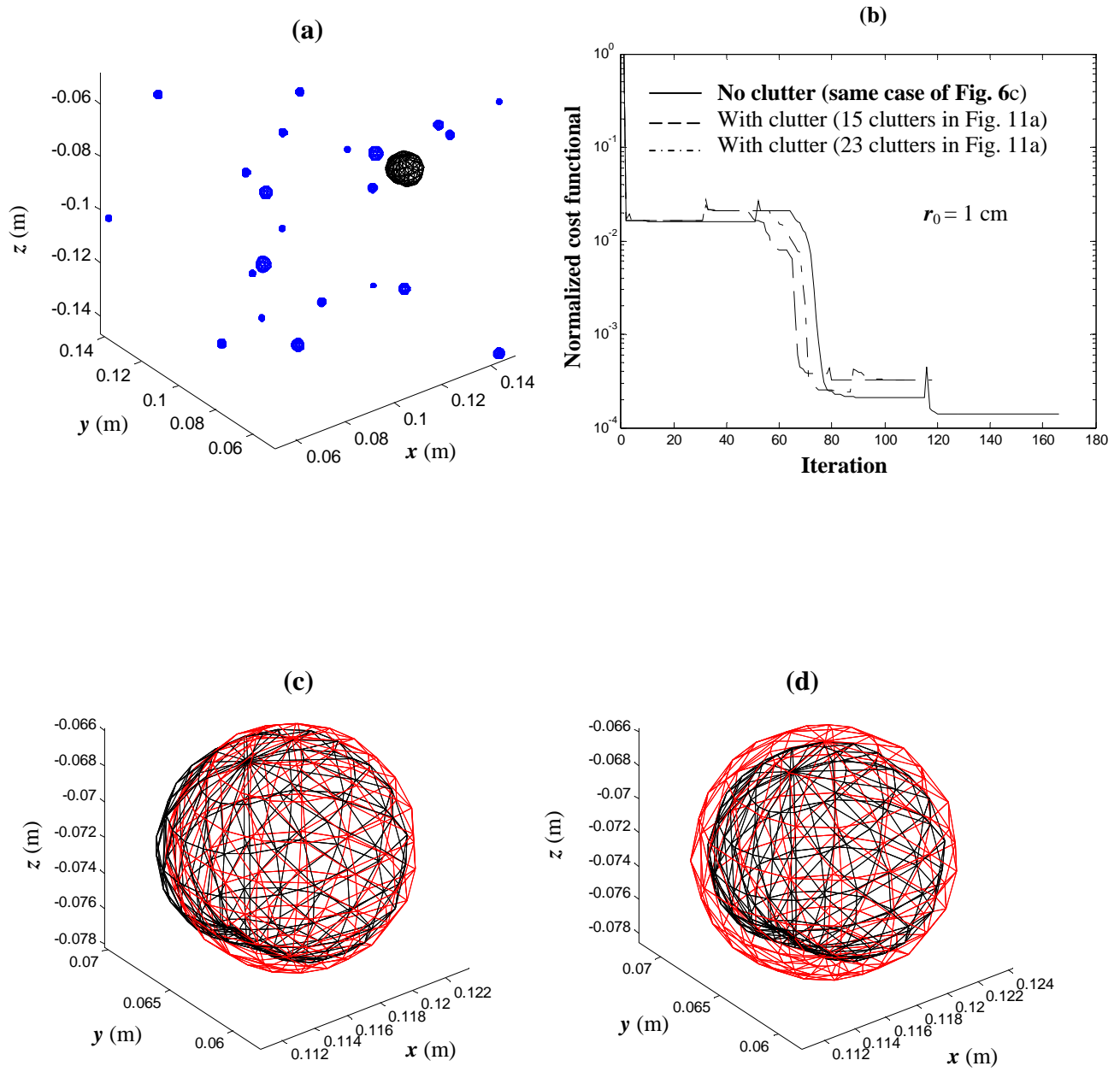


Fig. 11a-d